Critical Resolved Shear Stress and Work Hardening Determination in HCP Metals: Application to Zr Single Crystals

Jean-Sébastien Lecomte, Jérôme Crépin, Pierre Barberis

metals

MDPI

Article

Critical Resolved Shear Stress and Work Hardening Determination in HCP Metals: Application to Zr Single Crystals

Jean-Sébastien Lecomte [1,*], Jérôme Crépin [2] and Pierre Barberis [3]

[1] Université de Lorraine, CNRS, Arts et Métiers, LEM3, F-57000 Metz, France
[2] Centre des Matériaux Mines Paris, PSL University, BP 87, F-91003 Evry CEDEX, France; jerome.crepin@minesparis.psl.eu
[3] Framatome/CRC, F-73403 Ugine CEDEX, France; pierre.barberis@framatome.com
* Correspondence: jean-sebastien.lecomte@univ-lorraine.fr

Abstract: Obtaining precise parameters of deformation modes remains a significant challenge in materials science research. Critical resolved shear stresses (CRSS) and work hardening, particularly in hexagonal metals, are crucial parameters for constitutive laws in crystal plasticity. This paper presents a novel approach to determine CRSS and specific hardening matrix coefficients for commercially pure zirconium (α-Zr) at room temperature. In situ methods are employed to measure displacement fields using grids applied to the sample surface, while a comprehensive characterization of the activated deformation systems is performed via SEM and TEM. The CRSS for prismatic $\langle a \rangle$, pyramidal $\langle a \rangle$, and $\{10\bar{1}2\}$ and $\{11\bar{2}1\}$ twinning systems, as well as the self-hardening for prismatic slip and several work-hardening coefficients (for prismatic/prismatic and prismatic/pyramidal interactions), are reported in Zr single crystals. Finally, the results are compared with findings from the literature and atomistic simulations.

Keywords: HCP metals; work hardening; in situ tensile test; CRSS; zirconium

Citation: Lecomte, J.-S.; Crépin, J.; Barberis, P. Critical Resolved Shear Stress and Work Hardening Determination in HCP Metals: Application to Zr Single Crystals. *Metals* **2024**, *14*, 1101. https://doi.org/10.3390/met14101101

Academic Editor: Junting Luo

Received: 9 August 2024
Revised: 20 September 2024
Accepted: 20 September 2024
Published: 25 September 2024

1. Introduction

Zirconium is a strategic metal valued for its extremely low thermal neutron absorption, satisfactory mechanical properties, and excellent resistance to corrosion in high-temperature water—key attributes for its use in the nuclear industry. Zirconium (Zr) and its alloys are commonly used as cladding and fuel-rod materials in nuclear reactor cores [1]. At the crystal scale, α-Zr exhibits pronounced anisotropy in both its elastic and plastic properties [1–5]. A significant consequence of this anisotropy is the variation in thermal expansion coefficients and Young's moduli along the two principal direction ($\langle a \rangle$ and $\langle c \rangle$), leading to the development of internal stresses.

Due to its low symmetry, Zr exhibits more complex deformation mechanisms than cubic metals, with deformation modes not symmetrically distributed. The anisotropy in hexagonal close-packed (HCP) metals manifests in the following two ways:

- Intrinsic anisotropy: This arises from the atomic structure, resulting in different critical resolved shear stresses (CRSSs) for deformation mechanisms and varying strain-hardening values, as the interactions between systems are unequal.
- Extrinsic anisotropy: This comes from the pronounced texture of HCP metals, which significantly affects their macroscopic properties. Current models better account for this anisotropy through texture measurements [2,3,6].

The occurrence of slip on prismatic, pyramidal, or basal planes is typically linked to the corresponding critical resolved shear stresses (CRSSs). In hexagonal close-packed (HCP) metals, the relative ease of prismatic and basal slip is attributed to their low CRSS values and electronic structure, as well as the c/a ratio [7,8]. In HCP zirconium (α-Zr), where the c/a ratio is less than the ideal value, deformation occurs through a combination of slip and

twinning. The primary slip systems observed are (1) prismatic (P$\langle a \rangle$) and (2) pyramidal ($\pi_1\langle c+a \rangle$) [4,5] (refer to Table 1 for notation). To predict mechanical behavior after forming, current crystal plasticity models require key data, including CRSS and the work-hardening matrix. Prismatic slip (P$\langle a \rangle$) can be observed at all temperatures [9–12]. However, when stress is applied along the $\langle c \rangle$ axis, deformation is often accommodated by $\langle c+a \rangle$ slip, which activates five independent slip systems. This leads to a general, homogeneous strain without volume change [4,13–15]. Furthermore, the limited number of slip systems in zirconium can result in twinning, particularly at low temperatures (77 K) [11]. The following four types of twins are commonly observed in Zr at low temperatures: T1 and T2 tensile twins, as well as C1 and C2 compression twins, with the latter occurring at higher temperatures [16,17] (refer to Table 1 for notation).

Twinning is frequently observed during the compression of Zr single crystals along the $\langle c \rangle$ axis [2,18]. Tensile twins activate under tensile strain along the $\langle c \rangle$ axis, whereas compression twins emerge when compression strain is applied along this axis. Experimental studies of prismatic slip in α-Zr single crystals [11] have revealed similarities to single slip modes in face-centered cubic (FCC) crystals, particularly during the transition from stage I to stage II strain hardening [9]. In α-Zr crystals, oriented for prismatic slip, this behavior results from different velocities of edge and screw dislocation segments. Numerous researchers have studied Zr's plastic deformation. Akhtar [19] demonstrated that $\langle a \rangle$ dislocations on the prismatic plane dominate the deformation mechanism, with plasticity primarily driven by the motion of $\langle a \rangle$ screw dislocations, as the friction force on edge dislocations is minimal. These screw dislocations may deviate from their habit planes and glide on first-order pyramidal planes (π_1) or basal planes. Basal slip (B$\langle a \rangle$) is more difficult to activate, often requiring cross-slip of prismatic dislocations at room temperature [20,21], under high-strain deformation [22], or at temperatures above 850 K [23]. Through micropillar experiments and 3D dislocation modeling, Li [24,25] showed that cross-slip from P$\langle a \rangle$ to B$\langle a \rangle$ is controlled by long glissile segments on P$\langle a \rangle$ and jogs on B$\langle a \rangle$.

Table 1. Deformation modes considered in the present work. Planes and directions are expressed in the Miller–Bravais coordinate system.

Slip/Twin	Slip Plane Normal n^α	Slip Direction b^α	Notation
Basal	(0001)	$[1\bar{2}10]$	$B\langle a \rangle$
Prismatic	$(10\bar{1}0)$	$[1\bar{2}10]$	$P\langle a \rangle$
Pyramidal π_1	$(10\bar{1}1)$	$[\bar{1}2\bar{1}0]$	$\pi_1\langle a \rangle$
Pyramidal π_1	$(10\bar{1}1)$	$[2\bar{1}\bar{1}\bar{3}]$ or $[11\bar{2}\bar{3}]$	$\pi_1\langle c+a \rangle$
Pyramidal π_2	$(2\bar{1}\bar{1}2)$	$[2\bar{1}\bar{1}\bar{3}]$	$\pi_2\langle c+a \rangle$
Tension Twin	$\{10\bar{1}2\}$	$\langle 10\bar{1}1 \rangle$	T1
Tension Twin	$\{11\bar{2}1\}$	$\langle 11\bar{2}\bar{6} \rangle$	T2
Compression Twin	$\{2\bar{1}\bar{1}2\}$	$\langle 2\bar{1}\bar{1}\bar{3} \rangle$	C1
Compression Twin	$\{10\bar{1}1\}$	$\langle 10\bar{1}2 \rangle$	C2

Long segments of screw dislocations are observed in many zirconium single crystals, leading to the conclusion that edge dislocations move faster than screw dislocations. The gliding of screw segments is hindered by significant lattice friction, which results in dislocations that appear straight, indicating low mobility. It is well known that in hexagonal close-packed (HCP) metals, screw dislocations primarily dissociate in the prismatic plane and extend into the basal planes. These dissociated dislocations cannot glide in the prismatic planes, explaining the long screw dislocation segments observed in TEM. This phenomenon is known as the lock–unlock mechanism [21].

Atomistic simulations of dislocations [26], which average 3D dislocation cores, confirm the significant lattice frictional force acting on screw dislocations. Dislocation mobility is highly influenced by interstitial impurities [27]; for instance, Ferrer [28] demonstrated that the addition of just 25 ppm of sulfur reduces the creep rate of Zircaloy by a factor of three. Some single crystals display a phenomenon known as "pinning", where dislocation

motion is impeded by precipitates or atoms in solid solution, forming zigzag patterns. These findings highlight the strong interaction between mobile dislocations and impurities. Based on the chemical composition of these single crystals, the primary impurity is likely oxygen. These observations align with the work of Soo and Higgins, who demonstrated the effect of oxygen on the CRSS of prismatic slip [27]. Cross-slip and dislocation climb may serve as potential recovery mechanisms.

In this article, we describe a method for determining some hardening coefficients in zirconium single crystals at room temperature. The method relies on the interaction of two carefully selected slip systems. We perform in situ tensile testing inside a scanning electron microscope (SEM), which allows for the coupling of the evolution of local crystallographic orientation, as determined by electron backscattering diffraction (EBSD), with the evolution of local strain fields obtained through microextensometry using microgrids deposited on the tensile sample [29]. This technique enables the determination of local strain components $\left(\varepsilon_{11}^T, \varepsilon_{12}^T, \varepsilon_{21}^T, \varepsilon_{22}^T\right)$, where T denotes total strain). Activated systems are identified by SEM (via trace analysis), and postmortem thin foils from each single crystal are examined via transmission electron microscopy (TEM). With the aid of specialized software [30,31], Burgers vectors of dislocations, their characters (screw, edge, or mixed), and their glide planes are determined quickly and accurately. By knowing the deformation and the active system, it is possible to calculate the shear and resolved shear stress, and if the number of active systems is low, some coefficients of the hardening matrix can be obtained using the method described in the following section.

2. Methodology

2.1. Slip/Twin Systems

Deformation modes considered in the present work are given in Table 1.

2.2. Calculation of the Coefficients of the Work-Hardening Matrix

The resolved shear stress (RSS; τ_r^α) of a given slip system (α) is given by

$$\begin{aligned} \tau_r^\alpha &= \sum \sigma_{ij} \cdot m_{ij}^\alpha \\ \tau_r^\alpha &= \boldsymbol{\sigma} : \mathbf{m}^\alpha, \end{aligned} \tag{1}$$

where $\boldsymbol{\sigma}$ is the macroscopic true stress tensor and $\boldsymbol{m}^\alpha$ is the symmetric part of the Schmid tensor.

$$\mathbf{m}^\alpha = \frac{1}{2}(\mathbf{n}^\alpha \times \mathbf{b}^\alpha + \mathbf{b}^\alpha \times \mathbf{n}^\alpha), \tag{2}$$

with $\mathbf{n}^\alpha$ and $\mathbf{b}^\alpha$ representing the slip plane normal and the slip direction of the system (α), respectively. The rate of plastic deformation ($\dot{\varepsilon}_{ij}^P$) associated with the shear rate on the slip system (α) ($\dot{\gamma}^\alpha$) is given by

$$\text{if} \quad \begin{cases} \tau_r^\alpha \leq \tau_0^\alpha & \text{then} \quad \dot{\gamma}^\alpha = 0 \\ \tau_r^\alpha = \tau_0^\alpha & \text{then} \quad \dot{\gamma}^\alpha \geq 0 \end{cases} \tag{3}$$

$$\begin{aligned} \dot{\boldsymbol{\varepsilon}}^{\boldsymbol{P}} &= \sum_{\alpha=1}^{N} \dot{\gamma}^\alpha \, \mathbf{m}^\alpha \\ \dot{\boldsymbol{\varepsilon}}^P &= \sum_{\alpha=1}^{N} \frac{\dot{\gamma}^\alpha}{2}(\mathbf{n}^\alpha \times \mathbf{b}^\alpha + \mathbf{b}^\alpha \times \mathbf{n}^\alpha), \end{aligned} \tag{4}$$

where N is total number of activated slip systems. τ_0^α is the CRSS of system α, and τ_r^α is its resolved shear stress. For uniaxial tension along the **X** axis, the macroscopic stress tensor is expressed as follows:

$$\sigma_{ij} = \begin{pmatrix} \sigma_{11} & 0 & 0 \\ 0 & 0 & 0 \\ 0 & 0 & 0 \end{pmatrix}, \tag{5}$$

where $\sigma_{11} \neq 0$ and all other components are zero. At the onset of plasticity, τ_r^α corresponds to τ_0^α, which is noted as the CRSS.

The measurements of longitudinal deformation (ε_{11}^T) and transverse deformation (ε_{22}^T) are obtained using microgrid analysis, as explained in detail in [29]. This allows the total strain in both the longitudinal and transverse directions to be determined. Plastic deformation is then calculated using the following formula:

$$\begin{aligned} \varepsilon_{ij}^P &= \varepsilon_{ij}^T - \varepsilon_{ij}^e \\ \text{with} \quad \varepsilon_{ij}^e &= S_{ijkl}\sigma_{kl} \\ \boldsymbol{\varepsilon}^P &= \boldsymbol{\varepsilon}^T - \boldsymbol{\sigma}/E, \end{aligned} \tag{6}$$

where $E = \frac{1}{S_{1111}}$ is the Young's modulus, with S_{ijkl} representing the compliance tensor and ε^e and ε^T representing the elastic and total strain tensor, respectively.

At this stage, it is crucial to determine the activated slip systems, either through TEM or SEM, as detailed in the following section. At the onset of deformation, only one slip system is active. In our approach, we halt the process once two active systems, denoted as α and β, are identified. The resolved shear stresses (RSS; τ^α and τ^β) are calculated using Equation (1), while the shear strains (γ^α and γ^β) are determined according to Equation (4). Curves of τ vs. γ are then plotted. This allows for the resolved shear stress of each active slip system to be known, and solving the system of equations obtained from various experimental curves [(τ^α, γ^α), (τ^α, γ^β), (τ^β, γ^α), and (τ^β, γ^β)] yields the interaction coefficients between the slip systems.

The increase in the threshold stress of a system due to shear activity ($\Delta\gamma^\beta$) in the system is calculated as follows:

$$\Delta\tau_r^\alpha = \sum_{\beta=1}^{N} \left(\frac{\partial \tau_r^\alpha}{\partial \gamma^\beta} \right) \Delta\gamma^\beta = \sum_{\beta=1}^{N} h^{\alpha\beta} \Delta\gamma^\beta \tag{7}$$

where $\Delta\tau_r^\alpha$ is the increment of shear stress on the slip system (α) and $h^{\alpha\beta}$ is the work-hardening matrix.

This matrix expresses the work hardening caused in any system (α) by the plastic activity of a system (β). It can be interpreted by anisotropy of the interactions between slip systems.

At the first stage of the deformation (just α), one deduces $h^{\alpha\alpha}$ (*self*-hardening) thanks to the slope from the following curve (τ^α, γ^α)): $\Delta\tau_r^\alpha = h^{\alpha\alpha} \cdot \Delta\gamma^\alpha$.

At the second stage (activation of β), we obtain the following:

$$\begin{aligned} \dot{\varepsilon}_{11}^P &= m_{11}^\alpha \cdot \dot{\gamma}^\alpha + m_{11}^\beta \cdot \dot{\gamma}^\beta \\ \dot{\varepsilon}_{22}^P &= m_{22}^\alpha \cdot \dot{\gamma}^\alpha + m_{22}^\beta \cdot \dot{\gamma}^\beta \end{aligned} \tag{8}$$

and

$$\begin{aligned} \dot{\tau}_r^\alpha &= h^{\alpha\alpha} \cdot \dot{\gamma}^\alpha + h^{\alpha\beta} \cdot \dot{\gamma}^\beta \\ \dot{\tau}_r^\beta &= h^{\beta\alpha} \cdot \dot{\gamma}^\alpha + h^{\beta\beta} \cdot \dot{\gamma}^\beta \end{aligned} \tag{9}$$

The average of the slope allows for estimation of the coefficient values ($h^{\alpha\beta}$ and $h^{\beta\alpha}$) corresponding to work hardening between two slip systems. In Figure 1, the curves [(τ_i, γ_i),

$i = \alpha, \beta$] are schematized. Obtaining these graphs requires the resolution of a system of four equations with two unknown γ^α and γ^β values (Equations (8) and (9)).

The values of the s $h^{\alpha\beta}$ and $h^{\beta\alpha}$ coefficients result directly from the slopes of these curves (see Figure 1). One can write the following:

$$\begin{aligned} d\tau_r^\alpha &= A \cdot d\gamma^\alpha \quad \text{if} \quad d\gamma^\beta = 0 \\ d\tau_r^\alpha &= B \cdot d\gamma^\alpha \quad \text{if} \quad d\gamma^\beta > 0 \\ d\tau_r^\alpha &= C \cdot d\gamma^\beta \quad \text{if} \quad d\gamma^\beta > 0 \\ d\tau_r^\beta &= D \cdot d\gamma^\alpha \\ d\tau_r^\beta &= E \cdot d\gamma^\beta \end{aligned} \tag{10}$$

which yields the following (see detailed calculation in Appendix A):

$$h^{\alpha\beta} = \frac{(B - A) \cdot C}{B} \quad \text{and} \quad h^{\beta\alpha} = \frac{(D - A) \cdot E}{D} \tag{11}$$

Moreover $h^{\alpha\alpha} = A$, and if $\alpha = \beta$, then $h^{\alpha\alpha} = h^{\beta\beta}$.

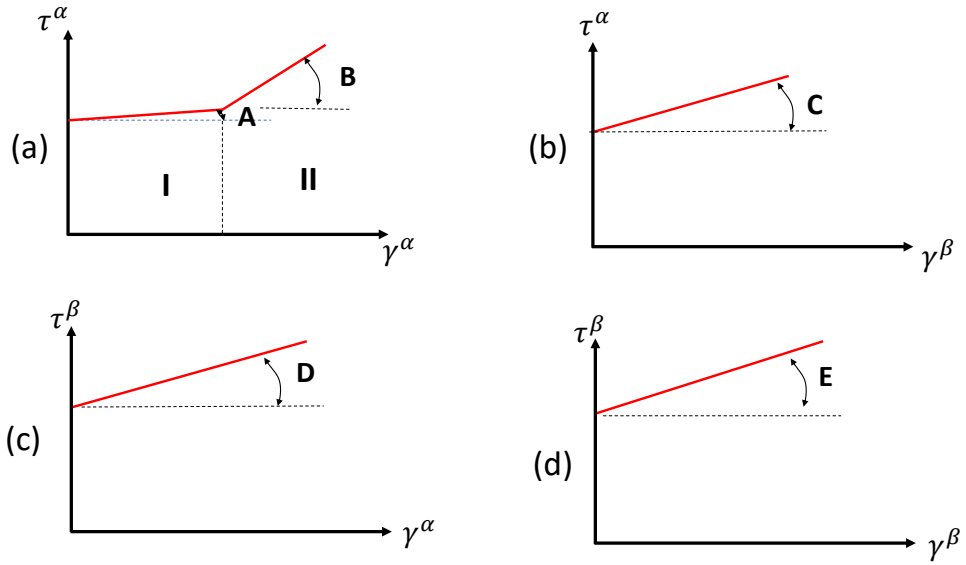

Figure 1. Schematic diagram of 4 different curves (τ^i, γ^i) with $i = \alpha, \beta$. (**a**) $(\tau^\alpha, \gamma^\alpha)$ HCP metals always exhibit low self-hardening (which is why A is represented as a low value) at stage I. From $d\gamma^\beta > 0$, it is stage II with the second active system and a higher slope (B). (**b**) $(\tau^\alpha, \gamma^\beta)$ curve and $d\tau_r^\alpha = C \cdot d\gamma^\beta$. (**c**) $(\tau^\beta, \gamma^\alpha)$ with $d\tau_r^\beta = D \cdot d\gamma^\alpha$. (**d**) $(\tau^\beta, \gamma^\beta)$ curve: $d\tau_r^\beta = E \cdot d\gamma^\beta$.

3. Experimental

High-purity Zr (99.95%) was obtained in the form of polycrystalline parallelepipeds (120 × 5 × 1 mm) with the chemical composition provided in Table 2. These bars underwent heat treatment at 850 °C for 5 days, followed by annealing at 700 °C for 24 h under secondary vacuum. This process resulted in centimetric grains.

Table 2. Chemical composition (weighted percent).

Zr	O_2	Fe	Hf
Balance	400 to 500 ppm	20 ppm	50 ppm

Single crystals with the appropriate crystallographic orientation were selected from within these parallelepipeds. The Euler angles of these single crystals, as measured by

EBSD, are provided in Table 3. The sample geometry consists of uniform parallelepipeds approximately 40 mm in length, with a gauge length of about 15 mm (see Figure 2). Additionally, the heads of the tensile samples were chosen from grains expected to maintain elastic behavior (smaller grain size and lower Schmid factor).

The experimental setup involves the use of an in situ tensile testing machine compatible with a SEM Jeol 845 (Akishima, Japan) (Figure 2). This setup allows for simultaneous coupling of the overall mechanical response of the samples (uniaxial stress measurement, deformation using traditional extensometry and microgrids [29], and crystallographic rotation through EBSD), with the observation of various mechanisms (identified via optical and electron images and EBSD).

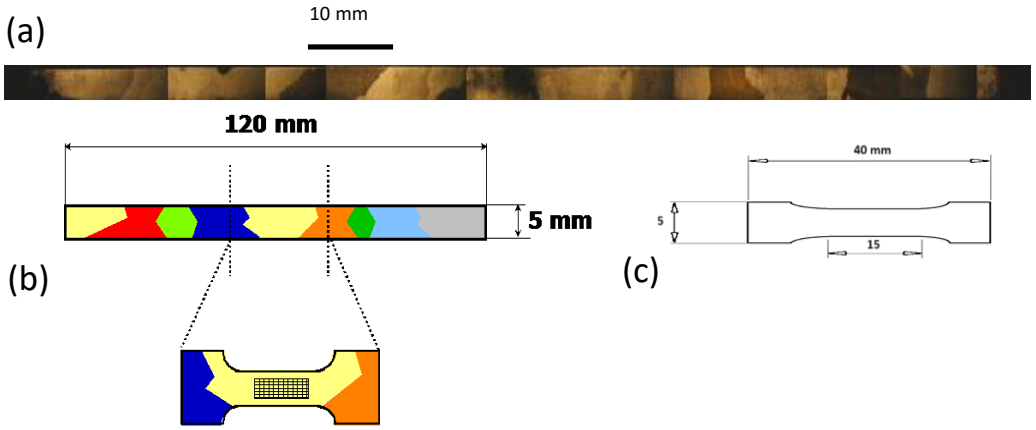

Figure 2. Micro tensile specimen (thickness = 1 mm) for EBSD and microgrid measurements. (**a**) Optical view; (**b**) sampling scheme; (**c**) specimens dimensions.

Table 3. Initial orientation of the studied single crystals of Zr. The Schmid factors in the case of uniaxial traction on the **X** axis are given for prismatic slip and for T1 twinning.

Name	φ_1 (°)	ϕ (°)	φ_2 (°)	SF $P\langle a \rangle$	SF $(10\bar{1}2)$
Zr1	336.00	86.13	315.08	0.4188	0.3451
Zr2	57.90	44.48	169.87	0.3156	0.1744
Zr3	98.21	85.85	111.51	0.0120	0.4878
Zr4	68.21	96.24	127.09	0.0719	0.4253
Zr5	42.27	74.58	141.26	0.2718	0.2109
Zr6	51.22	61.45	131.81	0.2646	0.2302
Zr8	5.44	56.95	91.47	0.4635	0.4058
Zr11	0.50	44.70	191.00	0.4959	0.4794

TEM investigations were performed with a CM200 Philips microscope (Cambridge, MA, USA) operating at 200 kV accelerating voltage and equipped with a CCD Slow Scan Gatan 791 camera (Pleasanton, CA, USA) for image and diffraction pattern acquisition.

Orientation measurements, as well as online help for the determination of the Burgers vectors and dislocations glide plane were performed by indexing Kikuchi patterns using homemade software named Euclid's Phantasies [30,31] (https://www.imim.pl/personal/adam.morawiec/A_Morawiec_Web_Page/downloads.html). The φ_1, ϕ, and φ_2 Euler angles correspond to the definition given by Bunge [32], and the crystal coordinate system is $(\mathbf{a_1} \parallel \mathbf{x})$ (see explanations in Appendix B).

Single crystals were metallographically prepared by mechanical polishing until a mirror polish was obtained, followed by electrochemical etching. Microgrids were deposited all along the useful surface area of the tensile sample [29]. The TEM samples were thinned by electropolishing using a Struers apparatus (TenuPol-5, Ballerup, Danemark) with an electropolishing solution containing 70% methanol, 20% monobutyl ether of ethylene glycol, and 10% perchloric acid (polishing conditions: 20 V at −30 °C). The thinned specimens

were quickly rinsed in methanol baths. The plane trace of a system (α) on the surface was calculated as the scalar product of the slip plane (n^α) and surface-normal $\mathbf{T}^\alpha$ ($\mathbf{n}^\alpha \cdot \mathbf{T}^\alpha = 0$; see Figure 3). The trace of the crystallographic plane in the observation plane, which satisfies the condition of $T_3^\alpha = 0$, is expressed as follows:

$$n_1^\alpha \cdot T_1^\alpha + n_2^\alpha \cdot T_2^\alpha = 0 \Rightarrow \frac{T_1^\alpha}{T_2^\alpha} = -\frac{n_2^\alpha}{n_1^\alpha}. \quad (12)$$

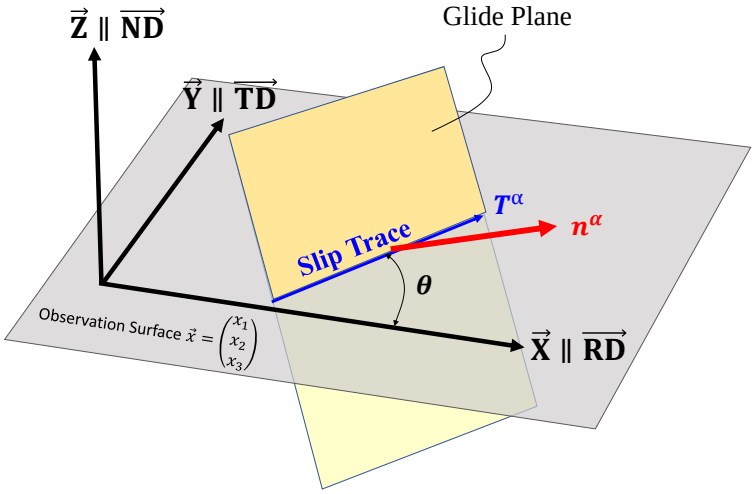

Figure 3. Determination of the glide system according to the angle of its trace.

Thus, the slip trace has an angle of $tan(\theta) = \left(\frac{T_1^\alpha}{T_2^\alpha}\right) = \left(-\frac{n_2^\alpha}{n_1^\alpha}\right)$ with n_1^α corresponding to not zero. A negative angle corresponds to the complementary quarter of the plane (left zone of the axis). This step can be conducted almost unambiguously, since there are only a few symmetries in a hexagonal lattice (in comparison to cubic lattice) and since a very few local crystal rotations were observed. The identification of dislocations by transmission electron microscopy (TEM) is based on the $\mathbf{g} \cdot \mathbf{b}$ invisibility criterion [33]. The image of a dislocation becomes invisible when it lies in the reflecting plane. The scalar product of the diffraction vector (**g**) and the Burgers vector (**b**) are then zero (for more details, the reader can refer to [34]). Twinning activity was analyzed with EBSD measurements using the MTEX v5.10 toolbox for MATLAB® [35] (https://mtex-toolbox.github.io/). Orientations were represented in pole figures on the **RD-TD** plane of the initial reference system and plotted with ATEX software [36] (http://www.atex-software.eu/).

4. Results

4.1. Stage I: Determination of Some CRSSs

In Figure 4a, the orientations of each single crystal are displayed in an inverse pole figure. By assuming equal CRSS for P$\langle a \rangle$ and T1 ($\tau_0^{P\langle a \rangle} \approx \tau_0^{\{10\bar{1}2\}}$), the active system between T1 and P$\langle a \rangle$ can be predicted. Figure 4b,c present the Schmid factors for P$\langle a \rangle$ and T1 individually. Different samples were deformed to Stage I (only one active slip system). The slip trace angle was measured in SEM, and each system was checked by TEM (Figure 5). The discrete measurements of crystal rotation (via EBSD) permits the calculation of the evolution of the Schmid factor to draw all the curves ($\tau^\alpha, \gamma^\alpha$).

In Figure 6 the stress–strain (σ, ε) curves of eight Zr single crystals are shown. Two categories of mechanisms appeared. Prismatic slip was observed on the Zr1, Zr2, Zr5, Zr6, Zr8, and Zr11 samples, and T1 twinning was observed on the Zr3 and Zr4 samples (see Figure 5).

In Table 4, the different mechanical properties are listed for each of the eight single crystals, including the Young's modulus (E), the yield stress (YS), and the ultimate tensile strength (UTS) .

Table 4. Summary table of the mechanical properties (experimental and theoretical Young's Modulus (E_{exp} and E_{theo}, respectively), Yield Stress (YS), strain rate ($\dot{\varepsilon}$), and ultimate tensile strength (UTS)).

Sample	E_{exp} [GPa] [1]	E_{theo} [GPa]	YS [MPa] [1]	$\dot{\varepsilon}$ [s^{-1}]	UTS [MPa] [1]
Zr1	101	81	60–82	2×10^{-4}	145.4
Zr2	80	111	80–85	2.5×10^{-4}	186.4
Zr3	72	94	277	8×10^{-5}	277.9
Zr4	77	110	234	4×10^{-5}	231.3
Zr5	58	82	78–110	3×10^{-4}	119.2
Zr6	132	81	125	4×10^{-5}	126.9
Zr8	108	84	181	2×10^{-4}	107.7
Zr11	144	110	134	8×10^{-5}	116

[1] These values were determined graphically.

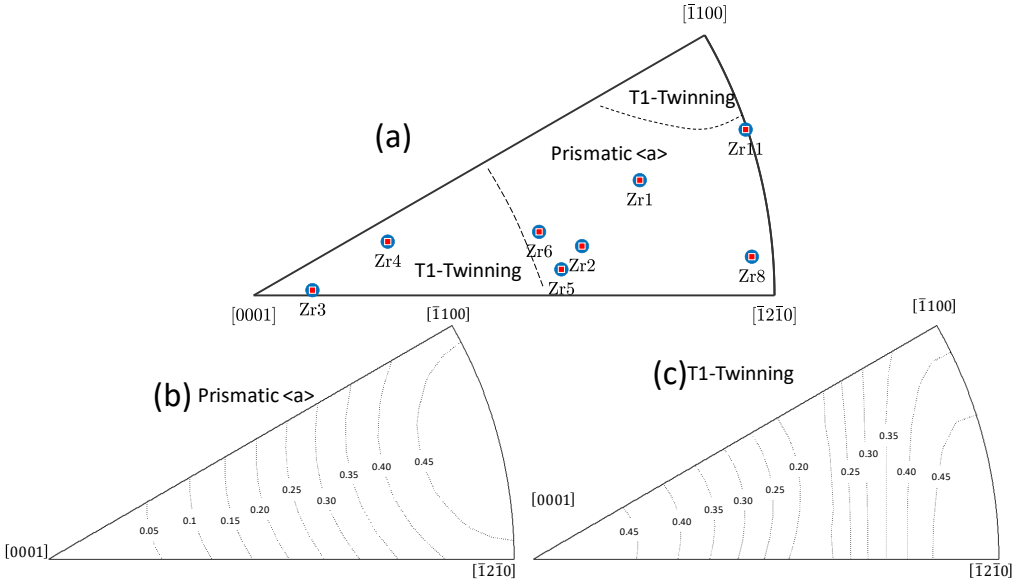

Figure 4. (**a**) Each orientation is localized in IPF linked with Table 3. The plot of the regions of the active systems (dotted line) of $P\langle a \rangle$ or the T1 twinning with the assumption that the CRSSs of the two systems are almost identical. (**b**,**c**) Schmid factor for prismatic $P\langle a \rangle$ and T1 twinning.

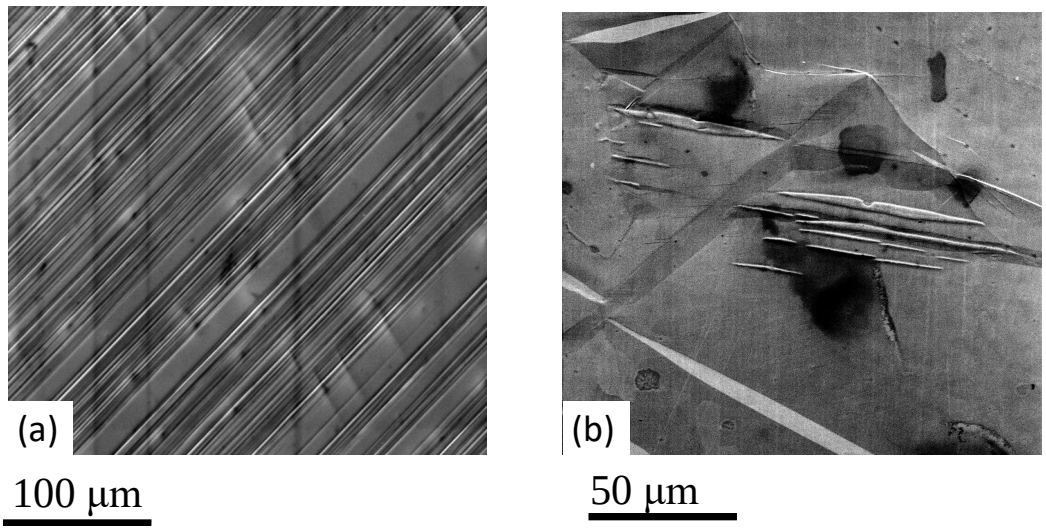

Figure 5. Some typical images of the observed mechanism. (**a**) Slip traces of P$\langle a \rangle$ (Zr1); (**b**) T1 twinning (in Zr3).

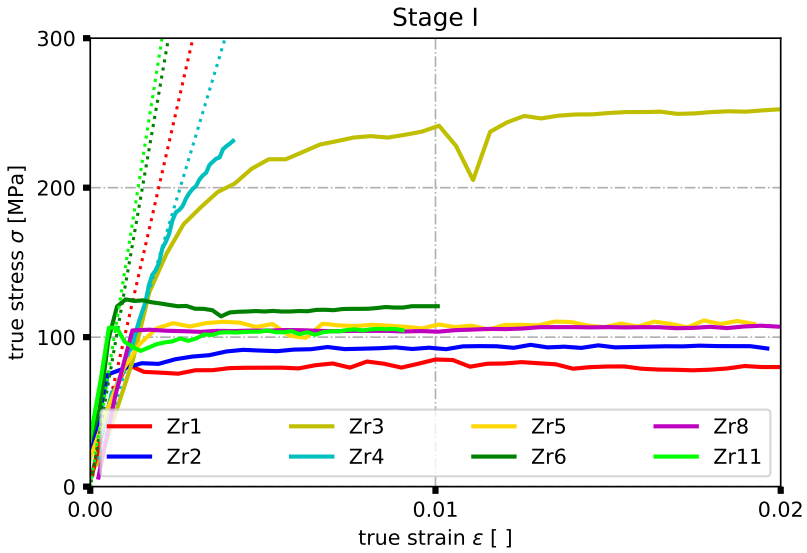

Figure 6. Curves (σ, ε) of 8 Zr singles crystals. Six samples exhibit a prismatic glide, except Zr3 and Zr4, which exhibit T1 twinning. The dashed lines are the slopes of the curves.

The elastic moduli and UTS and YS values were obtained graphically. The elastic modulus varies depending on the crystallographic orientation. We calculated the elastic moduli using the elastic constants provided by Fisher and Renken [37] and represented them on the IPF (Figure 7, along with the eight orientations of our single crystals. The high values of Zr8 and Zr11 can be explained by their orientations. The obtained results are in good agreement with the calculations.

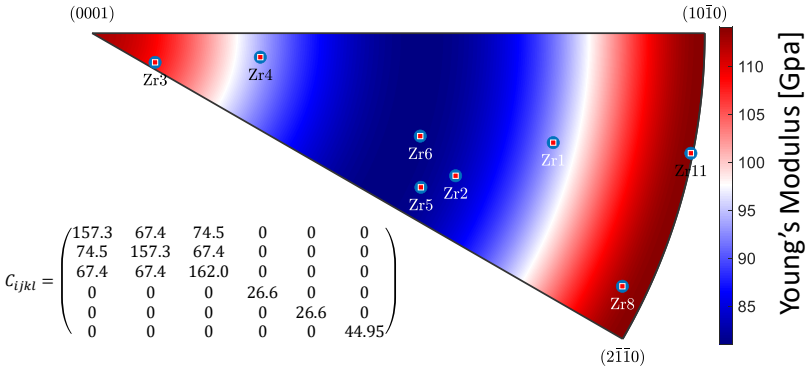

Figure 7. IPF of elastic moduli for Zr samples. Constants are taken from reference [37].

Every CRSS is compiled in Table 5. It can be seen from Figure 5a that slip lines are not homogeneously distributed; there are large areas without slip lines. Stage I is not homogeneous.

Table 5. Some values of CRSSs in Zr determined during this study.

P$\langle a \rangle$	**T1**	**T2**	$\pi_1\langle a \rangle$	$B\langle a \rangle$
40–45 MPa [1]	43 MPa [1]	110 MPa [2]	70 MPa [2]	$\geq$130 MPa [2]

[1] Determined with Stage I. [2] Determined with Stage II.

To illustrate the methodology explained above more clearly, Figure 8 presents the determination of parameters A, B, C, D, and E on the Zr2 single crystal.

4.2. Stage II: Interaction with Two or More Systems

The presence of two distinct hardening regimes, along with the fact that the change in slope coincides with the activation of the second prismatic slip system, suggests a

strong interaction between the two prismatic systems. This results in significant hardening. With increased deformation, the onset of double slip is observed (Figure 9a).

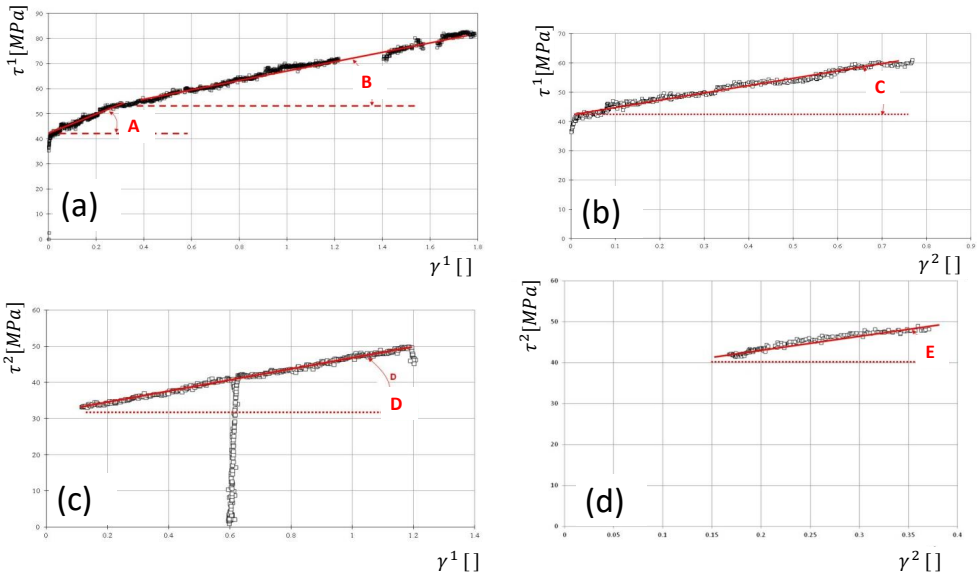

Figure 8. Example of hardening coefficients determined from the Zr2 sample. Here, A = 45.935, B = 17.459 (**a**), C = 24.582 (**b**), D = 18.616 (**c**), and E = 34.138 (**d**). $h^{\alpha\alpha}$ = 40.1 MPa, and $h^{\alpha\beta}$ = 50.1 MPa.

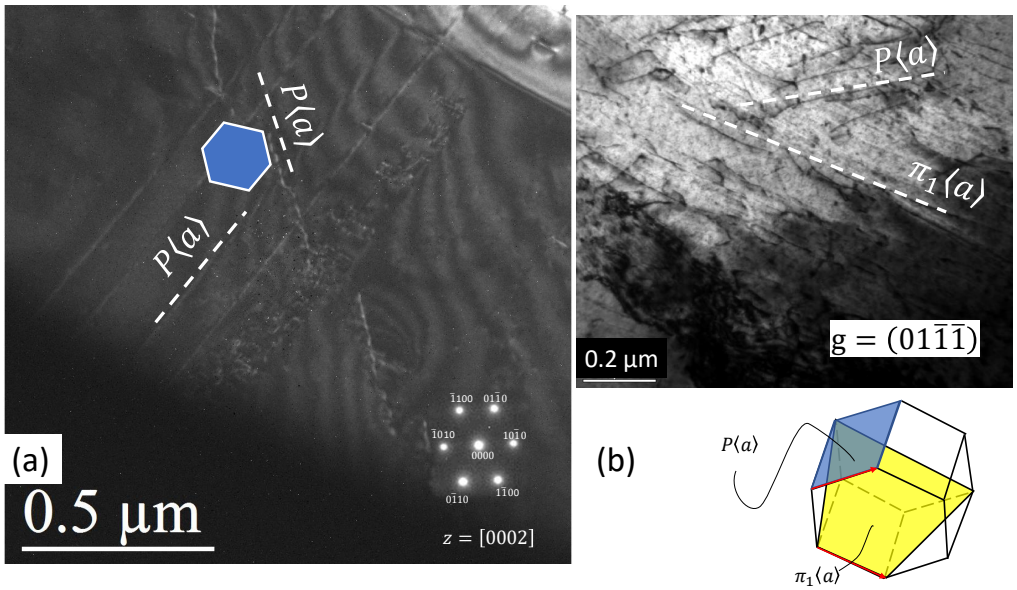

Figure 9. (**a**) TEM observations of the Zr2 sample (zone axis = [0002]; dark field on g = [10$\bar{1}$0]) (stage II): Two prismatic system are observed. (**b**) Zr5 sample: Two slips are determined ($\pi_1\langle a\rangle$ and $P\langle a\rangle$), with an oriented unit cell.

Pyramidal slip was observed on the Zr5 specimen (Figure 9b), and at the end of the deformation of the Zr8 specimen, it was characterized as being cross-slipped off the principal prismatic system towards the pyramidal system. T1 twinning was observed on the Zr3 and Zr4 samples (Figure 5b). T2 twinning was observed in Zr3. No C2 twining was observed in Zr because of the higher CRSS. Many researchers have reported that C2 twins can only form at elevated temperatures in Zr [38,39].

Determination of the work-hardening coefficient ($h^{\alpha\beta}$) requires the resolution of a set of two equations with two unknowns (α and β) and the measurement of ε_{11} and ε_{22}.

Uncertainty in ε_{11} measurement does not provide accurate values. In Table 6, the self-hardening component (h_{11}) and other components calculated in this study are given.

Figure 10c shows the distribution of the ε_{11} deformation to highlight the evolution of the heterogeneity of deformation. Indeed, at the first step, the value (equal to 1) does not have a physical direction, and the spectrum is extremely broad. There is, indeed, a factor of approximately 4 between the different areas (areas with and without slip traces, respectively). This means that the beginning of the deformation is highly heterogeneous at the local level. This heterogeneity may be due to a difference in distribution of interstitial atmospheres such as oxygen, which generates micro-variations in the CRSS. The histogram becomes more Gaussian with increasing deformation. The appearance of the Gaussian centered on the value of 1 means that the deformation is more homogeneous, reflecting the work-hardening effect. These observations are correlated with the TEM observation (Figure 5).

Table 6. Work-hardening values between the different prismatic systems.

$h^{\alpha\beta}$	$P\langle a_1\rangle$	$P\langle a_2\rangle$	$P\langle a_3\rangle$
$P\langle a_1\rangle$	13–123	180–238	180–238
$P\langle a_2\rangle$	180–238	13–123	180–238
$P\langle a_3\rangle$	180–238	180–238	13–123

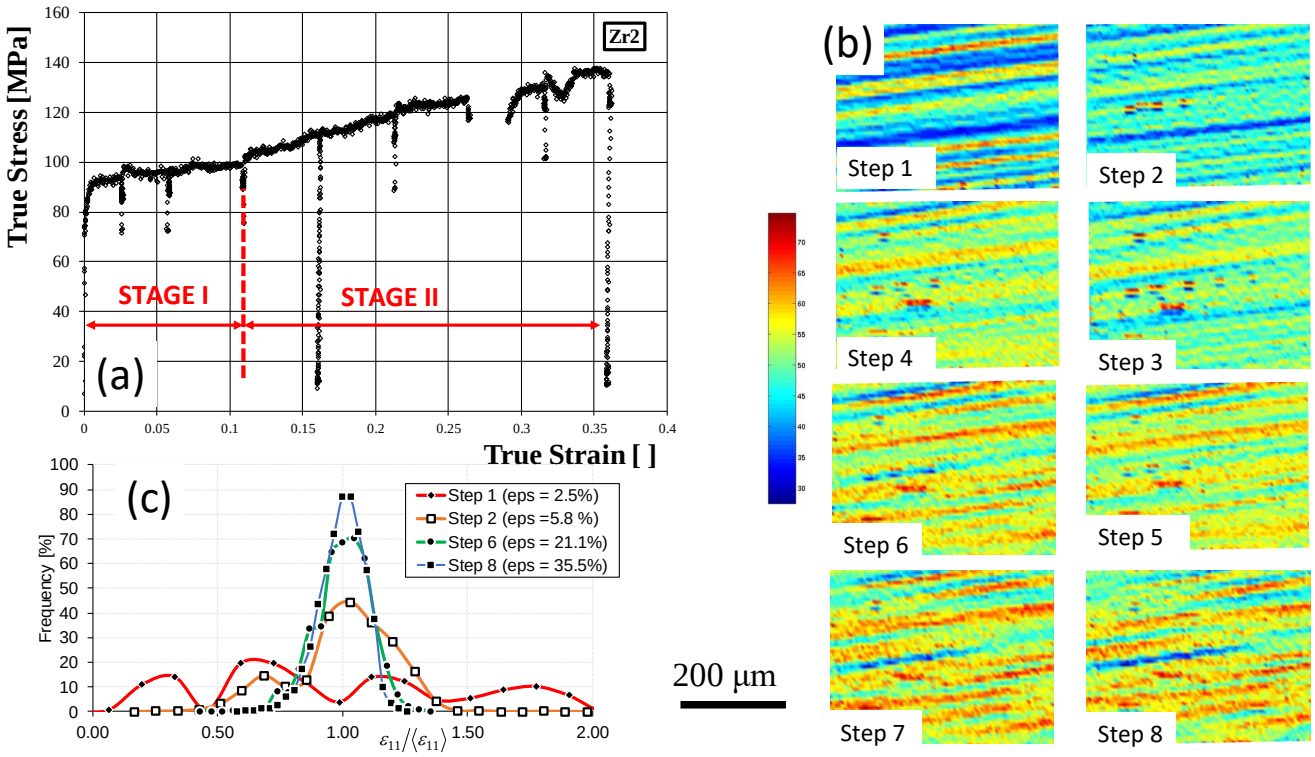

Figure 10. (**a**) Stress–strain curves of Zr2 with 8 steps. (**b**) ε_{11} strain field mapping according to the different steps (of Zr2). (**c**) Evolution of heterogeneity of the deformation ($\frac{\varepsilon_{11}}{\langle\varepsilon_{11}\rangle}$) with $\langle\varepsilon_{11}\rangle$ the mean deformation of ε_{11}.

For the Zr5 sample, the interaction between P$\langle a\rangle$ and $\pi_1\langle a\rangle$ was calculated, and the following values were found: $h^{\alpha\alpha}$ = 38 MPa, $h^{\alpha\beta}$ = 27.66 MPa, and $h^{\beta\alpha}$ = 4.57 MPa.

4.3. Influence of the Deformation Rate

The influence of the deformation rate on the CRSS of P$\langle a\rangle$ was studied. In Table 7, different orientations of single crystals are listed (Euler angles), as well as the inverse pole

figure of the studied single crystals. The orientations of single crystals dedicated to the velocity sensitivity tests for prismatic slip are illustrated on an inverse pole Figure 11.

Table 7. Orientation of the studied single crystals of Zr.

Name	φ_1 (°)	ϕ (°)	φ_2 (°)
Zr20	4.78	74.76	197.98
ZR21	121.26	105.52	337.23
Zr22	136.06	84.36	141.88
Zr23	173.93	71.96	248.96
Zr24	173.01	72.76	69.59

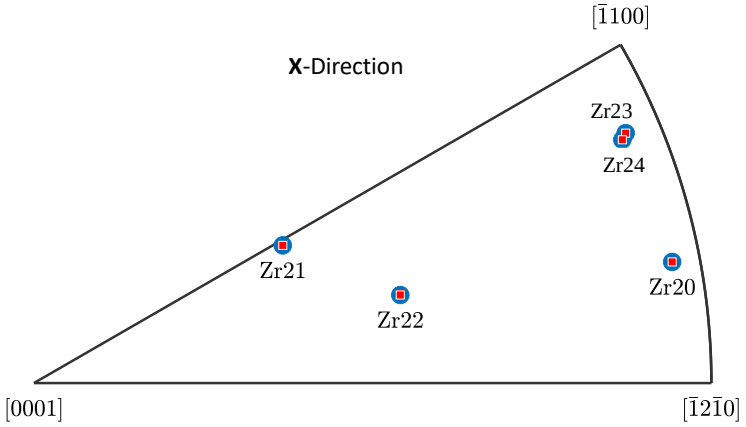

Figure 11. IPF from the Zr single crystals listed in Table 7.

The range of strain rate of our study extends from $\dot{\varepsilon} = 10^{-2}$–$10^{-6}$ s^{-1}, so it is considered quasi-static. In this range, the CRSS does not vary, as can be seen in Figure 12. In Table 8 the results obtained have been listed.

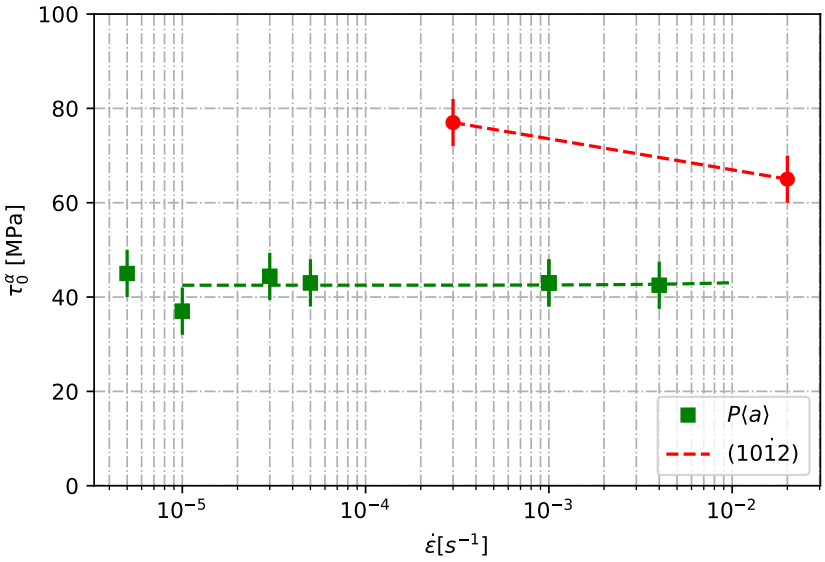

Figure 12. Evolution of the CRSS of $P\langle a\rangle$ vs. deformation rate (semi-logarithmic scale).

Table 8. Summary table of the mechanical properties of the 5 Zr-single crystals tested with different strain rates. Here, $\dot{\gamma} = \frac{\Delta\gamma}{\Delta t}$.

Sample	Strain Rate [s^{-1}] $\dot{\gamma}$	Yield Strength [MPa]	CRSS [MPa]
Zr20	1×10^{-3}	87	43
Zr21	3×10^{-5}	120	44.4
Zr22	5×10^{-6}	173	45
Zr23	1×10^{-5}	74	37
Zr24	5×10^{-5}	93	43

5. Discussion

5.1. Voce Law and Prismatic Glide

In Figure 13, we plot all the curves ($\tau - \Gamma$).

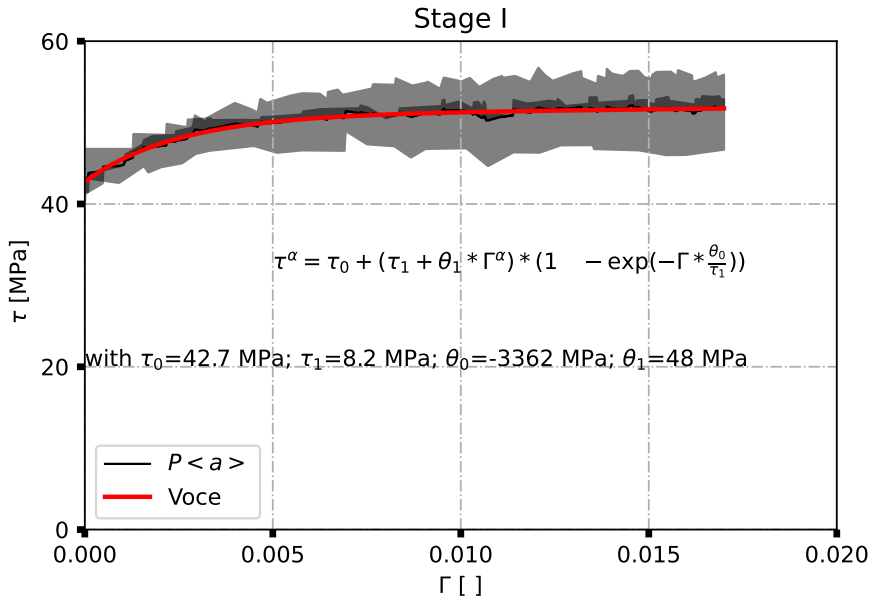

Figure 13. Adjustment of the $\tau(\Gamma)$ curves of the different $P\langle a \rangle$ systems with a Voce law, Adapted from Ref. [6].

The prismatic glide system curves ($\tau - \Gamma$) were fitted using the Voce law. In this case, Γ represents the accumulated shear strain ($\Gamma = \sum_i^N \gamma^i$, where N is the total number of active systems; see [6]). However, for the purpose of this study, we focus solely on Stage I, where only one slip system is active. Thus, $\Gamma = \gamma$.

$$\tau^\alpha = \tau_0 + (\tau_1 + \theta_1 * \Gamma^\alpha) * \left(1 - \exp\left(-\Gamma^\alpha \frac{\theta_0}{\tau_1}\right)\right), \tag{13}$$

where τ_0 = 42.7 MPa, τ_1 = 8.2 MPa, $\theta_0 = -3362$ MPa, and θ_1 = 48 MPa.

5.2. Deformation Rate

As can be seen in Figure 12, the effect of the deformation rate on the critical resolved shear stress (CRSS) for prismatic $\langle a \rangle$ slip is minimal, contrary to the findings of Pujol [40]. Soo and Higgins [27] observed that oxygen additions significantly increase the temperature dependence of the yield stress in zirconium, especially at low temperatures, and noted a Cottrell–Stokes phenomenon when $O_2 \geq 2000$ ppm. In this study, the Zr samples contained approximately 400 ppm of oxygen.

Research on zirconium is limited and primarily focuses on the CRSS for prismatic $\langle a \rangle$ slip; we compiled these studies in Figure 14. We observe that the CRSS for P$\langle a \rangle$ with 400 ppm of O_2 is in excellent agreement with the results reported by other researchers [11,18,27,41,42].

In Figure 15, a TEM image of Zr5 is compared with a simulation conducted by Monnet [43]. Monnet's dislocation dynamics simulations, based on several key assumptions—(1) a microstructure dominated by $\langle a \rangle$ screw dislocations, (2) the predominance of prismatic slip systems, (3) high sensitivity to oxygen, and (4) a yield strength strongly dependent on temperature—are consistent with our TEM observations.

TEM observations (see Figure 16) revealed cross-slip from the prismatic to the basal plane at room temperature, involving straight screw dislocations moving via a kink-pair mechanism.

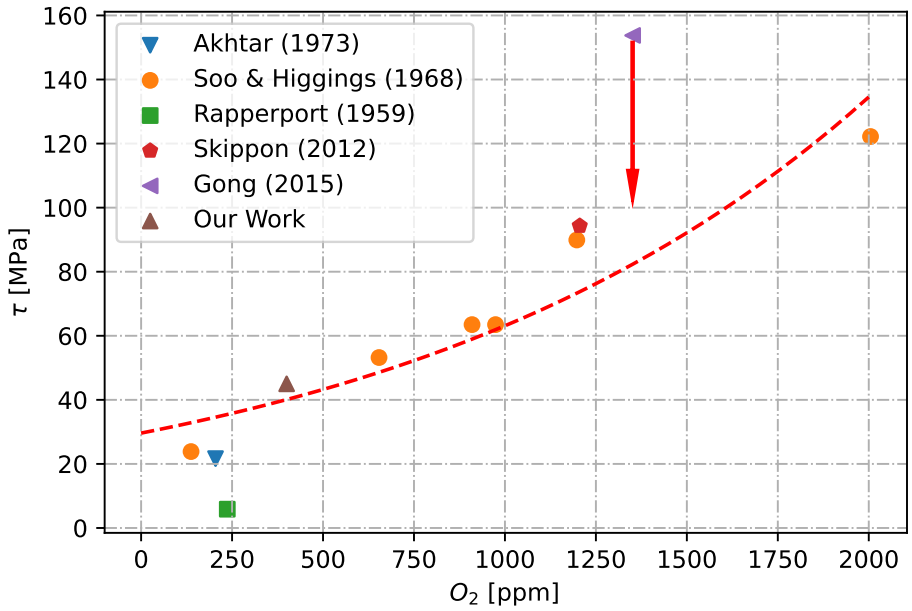

Figure 14. Effect of oxygen equivalent concentration on CRSS value for P$\langle a \rangle$ slip in commercially pure Zr and zircaloy-2, Adapted from Refs. [11,18,27,41,42]. The higher value obtained by Gong [42] micro-beams is probably due to FIB damage.

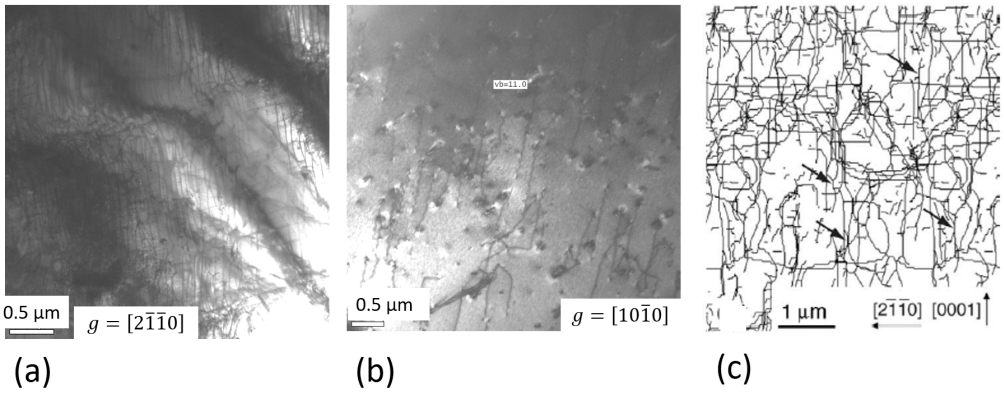

Figure 15. (**a**) TEM image obtained of Zr5 g = $[2\bar{1}\bar{1}0]$. (**b**) Same area but with g = $[10\bar{1}0]$. (**c**) Simulation under the same diffraction conditions, Reprinted with permission from Ref. [43]. Copyright 2004, Copyright Elsevier.

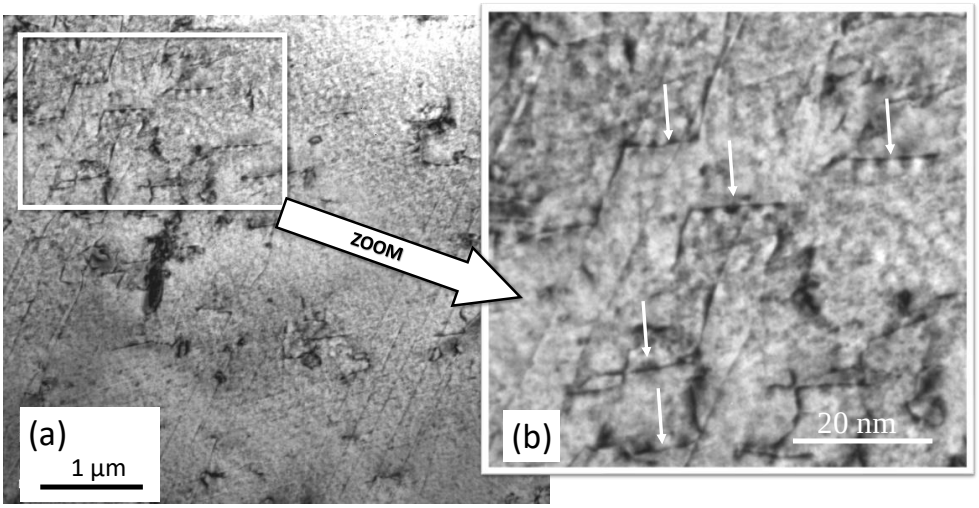

Figure 16. (**a**) TEM bright-field image of Zr5 sample (g = $[\bar{1}101]$). (**b**) White arrows indicate cross-slip. $\langle a \rangle$ dislocations in the prismatic plane cross on the basal plane.

6. Conclusions

A method was developed herein to calculate certain coefficients of the hardening matrix. This approach combines in situ SEM-EBSD tests to track crystal rotations with microgrids to obtain displacement fields. Postmortem observations of slip traces in SEM, along with detailed identification of dislocation types using TEM, were also conducted.

At room temperature, critical resolved shear stresses (CRSSs) for various deformation modes in zirconium (with 400 ppm O_2) were evaluated as follows:

$$\tau_0^{P\langle a\rangle} = 40 \text{ MPa}; \quad \tau_0^{\{10\bar{1}2\}} = 43 \text{ MPa}; \quad \tau_0^{\{11\bar{2}1\}} = 110 \text{ MPa};$$

$$\tau_0^{\pi_1\langle a\rangle} = 70 \text{ MPa}; \quad \text{and} \quad \tau_0^{B\langle a\rangle} > 130 \text{ MPa}$$

In the tested strain-rate range, no noticeable change in CRSS for prismatic P$\langle a \rangle$ slip was observed. This serves as indirect evidence that a higher oxygen content is required to detect such changes. Testing zirconium with higher oxygen content (>2000 ppm O_2) is necessary, as oxygen atoms act as pinning points for dislocation movement. A sufficient amount is needed to significantly increase lattice friction. This is the first study to focus on the strain-hardening coefficient. Previously, we shared some of our results with a French research team, and they successfully modeled our experimental data [43] (see Figure 15a,c). The developed method is applicable to all hexagonal metals (such as titanium, zinc, and magnesium) and, more broadly, to all metals, as long as no more than two active slip systems are considered at the same time.

Author Contributions: J.C.: formal analysis, data curation, investigation, methodology, software, visualization, and writing—review and editing. P.B.: funding acquisition, investigation, methodology, project administration, supervision, validation, and writing—review and editing. J.-S.L.: conceptualization, formal analysis, funding acquisition, investigation, methodology, project administration, resources, supervision, software, visualization, and writing—original draft. All authors have read and agreed to the published version of the manuscript.

Funding: This research received no external funding.

Data Availability Statement: The original contributions presented in the study are included in the article, further inquiries can be directed to the corresponding author.

Acknowledgments: J.-S.L. thanks Daniel Caldemaison for the gold grid deposit.

Conflicts of Interest: Author Pierre Barberis was employed by the Framatome/CRC. The remaining authors declare that the research was conducted in the absence of any commercial or financial relationships that could be construed as a potential conflict of interest.

Appendix A. Calculation of Slopes A, B, C, D, and E

The increase in the threshold stress ($\Delta\tau_r$) of a system (α) due to shear activity ($\Delta\gamma^\beta$) is calculated as follows [6]:

$$\Delta\tau_r^\alpha = \sum_{\beta=1}^{N}\left(\frac{\partial\tau_r^\alpha}{\partial\gamma^\beta}\right)\Delta\gamma^\beta = \sum_{\beta=1}^{N} h^{\alpha\beta}\Delta\gamma^\beta \tag{A1}$$

where $\Delta\tau_r^\alpha$ is the increment of shear stress on the slip system (α) and $h^{\alpha\beta}$ is the work-hardening matrix.

$$\Delta\tau_r^\alpha = h^{\alpha\alpha}\cdot\Delta\gamma^\alpha + h^{\alpha\beta}\cdot\Delta\gamma^\beta \tag{A2}$$

$$\Delta\tau_r^\beta = h^{\beta\alpha}\cdot\Delta\gamma^\alpha + h^{\beta\beta}\cdot\Delta\gamma^\beta \tag{A3}$$

Referring to Figure 1,

$$\Delta\tau_r^\alpha = A\cdot\Delta\gamma^\alpha \quad \text{if} \quad \Delta\gamma^\beta = 0 \tag{A4}$$

$$\Delta\tau_r^\alpha = B\cdot\Delta\gamma^\alpha \quad \text{if} \quad \Delta\gamma^\beta > 0 \tag{A5}$$

$$\Delta\tau_r^\alpha = C\cdot\Delta\gamma^\beta \quad \text{if} \quad \Delta\gamma^\beta > 0 \tag{A6}$$

$$\Delta\tau_r^\beta = D\cdot d\gamma^\alpha \tag{A7}$$

$$\Delta\tau_r^\beta = E\cdot\Delta\gamma^\beta \tag{A8}$$

From Equations (A2) and (A4),

$$\Delta\tau_r^\alpha = \mathrm{A}\cdot\Delta\gamma^\alpha \Rightarrow \mathrm{A} = \frac{\Delta\tau^\alpha}{\Delta\gamma^\alpha} = h^{\alpha\alpha} \tag{A9}$$

From Equation (A5),

$$\Delta\tau_r^\alpha = \mathrm{B}\cdot\Delta\gamma^\alpha \Rightarrow \Delta\gamma^\alpha = \frac{\Delta\tau_r^\alpha}{\mathrm{B}} \tag{A10}$$

From Equation (A6),

$$\Delta\tau_r^\alpha = \mathrm{C}\cdot\Delta\gamma^\beta \Rightarrow \Delta\gamma^\beta = \frac{\Delta\tau_r^\alpha}{\mathrm{C}} \tag{A11}$$

Replacing Equations (A9)–(A11) in Equation (A2) yields the following:

$$\Delta\tau_r^\alpha = \mathrm{A}\cdot\frac{\Delta\tau_r^\alpha}{\mathrm{B}} + h^{\alpha\beta}\cdot\frac{\Delta\tau_r^\alpha}{\mathrm{C}} \tag{A12}$$

Simplifying Equation (A12) with $\Delta\tau_r^\alpha$ yields the following:

$$1 = \frac{A}{B} + \frac{h^{\alpha\beta}}{C} \Rightarrow h^{\alpha\beta} = \mathrm{C}\left(1 - \frac{A}{B}\right) \tag{A13}$$

Assumption A1. *Same glide systems* $\Rightarrow h^{\beta\beta} = h^{\alpha\alpha} = A$.

From Equations (A3) and (A7),

$$\Delta\tau_r^\beta = \mathrm{D}\cdot\Delta\gamma^\alpha \Rightarrow \Delta\gamma^\alpha = \frac{\Delta\tau_r^\beta}{\mathrm{D}} \tag{A14}$$

From Equation (A8),

$$\Delta\tau_r^\beta = \mathrm{E}\cdot\Delta\gamma^\beta \Rightarrow \Delta\gamma^\beta = \frac{\Delta\tau_r^\beta}{\mathrm{E}} \tag{A15}$$

Replacing Equations (A3), (A14), and (A15) in Equation (A12) yields the following:

$$\Delta\tau_r^\beta = h^{\beta\alpha}\cdot\frac{\Delta\tau_r^\beta}{\mathrm{D}} + \mathrm{A}\cdot\frac{\Delta\tau_r^\beta}{\mathrm{E}} \tag{A16}$$

Simplifying Equation (A16) with $\Delta\tau_r^\beta$ yields the following:

$$1 = \frac{h^{\beta\alpha}}{D} + \frac{A}{E} \Rightarrow h^{\beta\alpha} = D\left(1 - \frac{A}{E}\right) \tag{A17}$$

Assumption A2. *The glide systems are not the same, but* $h^{\alpha\beta} = h^{\beta\alpha}$.

Replacing Equations (A14) and (A15) in Equation (A3) yields the following:

$$\Delta\tau_r^\beta = h^{\alpha\beta}\cdot\left(\frac{\Delta\tau_r^\beta}{\mathrm{D}}\right) + h^{\beta\beta}\cdot\left(\frac{\Delta\tau_r^\beta}{\mathrm{E}}\right) \tag{A18}$$

Simplifying Equation (A18) with $\Delta\tau_r^\beta$ yields the following:

$$1 = \frac{h^{\alpha\beta}}{\mathrm{D}} + \frac{h^{\beta\beta}}{\mathrm{E}} \Rightarrow h^{\beta\beta} = E\left(1 - \frac{h^{\alpha\beta}}{D}\right) \tag{A19}$$

Replacing $h^{\alpha\beta}$ with Equation (A17) in Equation (A19) yields the following:

$$h^{\beta\beta} = \frac{E}{D}\left(D - C\left(1 - \frac{A}{B}\right)\right) \tag{A20}$$

Appendix B. Geometry of HCP Crystal

The primitive hexagonal unit cell has axes of $\boldsymbol{a_1} = \boldsymbol{a_2} \neq \boldsymbol{c}$ and corresponding angles of $\alpha = \beta = 90°, \gamma = 120°$. Hexagonal basis H $(\boldsymbol{a_1}, \boldsymbol{a_2}, \boldsymbol{a_3}, \boldsymbol{c})$ is based on four crystallographic axes and four indices (*Weber symbols*), one of which is redundant (Figure A1).

$$\boldsymbol{a_1} + \boldsymbol{a_2} + \boldsymbol{a_3} = 0 \tag{A21}$$

Let $(HKL)\langle UVW\rangle$ represent Miller indices. In the HCP structure, we have the following notation: $(hkil)\langle uvtw\rangle$ with $i = -(h+k)$ and $u = \frac{2U-V}{3}$; $v = \frac{2V-U}{3}$; $w = W$ so $U = 2u + v$; $V = u + 2v$ and $W = w$.

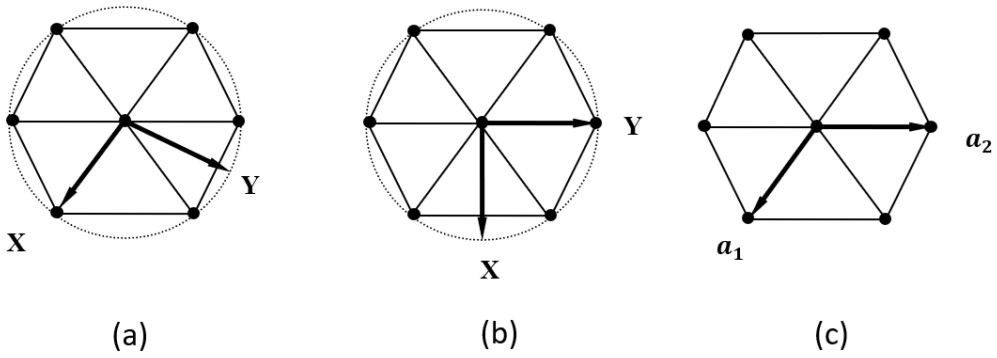

Figure A1. Three possibilities of the basis for the hexagonal structure. (**a**) International orthonormal basis with $(\boldsymbol{a_1} \parallel \mathbf{X})$. (**b**) Orthonormal basis with $(\boldsymbol{a_2} \parallel \mathbf{Y})$. (**c**) Hexagonal basis $(\boldsymbol{a_1}, \boldsymbol{a_2}, \boldsymbol{a_3}, \boldsymbol{c})$.

Let **r** be a vector in hexagonal basis H $(\boldsymbol{a_1}, \boldsymbol{a_2}, \boldsymbol{a_3}, \boldsymbol{c})$ and **v** be the same vector but expressed in an orthonormal basis (E) **(X, Y, Z)** (the notation is as follows: the change in basis matrix, which changes the indices of the planes and directions of basis E to those of basis H, is denoted as $(E\boldsymbol{T}H)$; a vector **(r)** expressed in basis H is denoted as $[H, \boldsymbol{r}]$). For more details, see [44].

$$\begin{aligned} \boldsymbol{v} &= [E, \boldsymbol{v}] = (E\boldsymbol{T}H)[H, \boldsymbol{r}] \\ \boldsymbol{r} &= U \cdot a_1 + V \cdot a_2 + W \cdot c \\ \boldsymbol{v} &= x \cdot \boldsymbol{X} + y \cdot \boldsymbol{Y} + z \cdot \boldsymbol{Z} \end{aligned} \tag{A22}$$

Several conventions are used with regard to reference bases associated with hexagonal lattice; either the international basis $(\boldsymbol{a_1} \parallel \mathbf{X})$ or the reference system is usually used in textures $(\boldsymbol{a_2} \parallel \mathbf{Y})$, which implies a rotation of 30° on the **c** axis.

The coordinate transformations $(E\ \boldsymbol{T}H)$ are given in the cases of both $(\boldsymbol{a_1} \parallel \mathbf{X})$ and $(\boldsymbol{a_2} \parallel \mathbf{Y})$.

Case 1: $(\boldsymbol{a_1} \parallel \mathbf{X})$

$$\boldsymbol{A}'_4 = (E\ \boldsymbol{T}H) = \begin{bmatrix} 1 & -1/2 & 0 \\ 0 & \sqrt{3}/2 & 0 \\ 0 & 0 & c/a \end{bmatrix}$$

Case 2 : $(\boldsymbol{a_2} \parallel \mathbf{Y})$

$$\boldsymbol{A}_4 = (E\ \boldsymbol{T}H) = \begin{bmatrix} \sqrt{3}/2 & 0 & 0 \\ -1/2 & 1 & 0 \\ 0 & 0 & c/a \end{bmatrix}$$

Passing from the hexagonal basis (4 indices) to the orthonormal basis (with $(\boldsymbol{a_2} \parallel \mathbf{Y})$) is expressed by the following equations (indices are explained in Table 1). Table A1 uses notations for a plane and a direction in HCP.

$$\begin{bmatrix} U \\ V \\ W \end{bmatrix} = \begin{bmatrix} \sqrt{3} & \sqrt{3}/2 & 0 \\ 0 & 3/2 & 0 \\ 0 & 0 & c/a \end{bmatrix} \begin{bmatrix} u \\ v \\ w \end{bmatrix} \tag{A23}$$

$$\begin{bmatrix} H \\ K \\ L \end{bmatrix} = \begin{bmatrix} 2/\sqrt{3} & 1/\sqrt{3} & 0 \\ 0 & 1 & 0 \\ 0 & 0 & a/c \end{bmatrix} \begin{bmatrix} h \\ k \\ l \end{bmatrix} \tag{A24}$$

where a and c are the parameters of the hexagonal unit cells.

Table A1. 4-Index (Miller-Bravais) and 3-Index (Miller) for directions and planes.

System	Orthonormal Basis E	Hexagonal Basis H (4 Indices)
Direction	$\begin{bmatrix} U \\ V \\ W \end{bmatrix}$	$\begin{bmatrix} u \\ v \\ t \\ w \end{bmatrix}$
Plane	$\begin{bmatrix} H \\ K \\ L \end{bmatrix}$	$\begin{bmatrix} h \\ k \\ i \\ l \end{bmatrix}$

References

1. Tenckhoff, E. *Deformation Mechanisms, Texture, and Anisotropy in Zirconium and Zircaloy*; ASTM International: West Conshohocken, PA, USA, 1988; Volume 966. [CrossRef]
2. Proust, G.; Tomé, C.; Kaschner, G. Modeling texture, twinning and hardening evolution during deformation of hexagonal materials. *Acta Mater.* **2007**, *55*, 2137–2148. [CrossRef]
3. Van Houtte, P. The effect of strain path on texture: Theoretical and experimental considerations. In *Strength of Metals and Alloys (ICSMA 7)*; Elsevier: Amsterdam, The Netherlands, 1986; pp. 1701–1725. [CrossRef]
4. Akhtar, A. Prismatic slip in zirconium single crystals at elevated temperatures. *Metall. Trans. A* **1975**, *6*, 1217–1222. [CrossRef]

5. Naka, S.; Lasalmonie, A. Cross-slip on the first order pyramidal plane (10 1) of a-type dislocations [1 10] in the plastic deformation of α-titanium single crystals. *J. Mater. Sci.* **1983**, *18*, 2613–2617. [CrossRef]
6. Tome, C.N.; Lebensohn, R.A. *Material Modeling with the Visco-Plastic Self-Consistent (VPSC) Approach: Theory and Practical Applications*; Elsevier: Amsterdam, The Netherlands, 2023. [CrossRef]
7. Legrand, B. Relation between the electronic structure and ease of gliding in hexagonal close-packed metals. *Philos. Mag. B.* **1984**, *49*, 171–184. [CrossRef]
8. Clouet, E. Screw dislocation in zirconium: An ab initio study. *Phys. Rev. B—Condensed Matter Mater. Phys.* **2012**, *86*, 144104. [CrossRef]
9. Trojanová, Z.; Lukáč, P. Thermally activated deformation of alpha zirconium. *Cryst. Res. Technol.* **1984**, *19*, 401–405. [CrossRef]
10. Miyada-Naborikawa, L.; De Batisi, R.; Delavignette, P. Transmission electron microscopy observations of dislocations and twins in polycrystalline zirconium. *Phys. Status Solidi (a)* **1985**, *89*, 521–531. [CrossRef]
11. Rapperport, E. Room temperature deformation processes in zirconium. *Acta Metall.* **1959**, *7*, 254–260. [CrossRef]
12. MacEwen, S.; Fleck, R.; Ho, E.; Woo, O. Deformation of α-zirconium in the vicinity of 0.5 Tm. *Metall. Trans. A* **1981**, *12*, 1751–1759. [CrossRef]
13. Crépin, J. Etude des Mécanismes de Déformation et D'endommagement du Zirconium Grade 702 Traité beta: Application aux Cordons de Soudure. Ph.D. Thesis, Ecole Polytechnique, Palaiseau, France, 1995.
14. Onchi, T.; Kayano, H.; Higashiguchi, Y.; Narui, M. Effects of temperature, strain rate, and specimen orientation on localized plastic deformation of irradiated zircaloy-2. *J. Nucl. Sci. Technol.* **1980**, *17*, 848–856. [CrossRef]
15. Kaschner, G.; Tomé, C.; Beyerlein, I.; Vogel, S.; Brown, D.; McCabe, R. Role of twinning in the hardening response of zirconium during temperature reloads. *Acta Mater.* **2006**, *54*, 2887–2896. [CrossRef]
16. Murty, K.; Adams, B. Multiaxial creep of textured Zircaloy-4. In *Mechanical Testing for Deformation Model Development*; ASTM International: West Conshohocken, PA, USA, 1982. [CrossRef]
17. Murty, K.L.; Charit, I. Texture development and anisotropic deformation of zircaloys. *Prog. Nucl. Energy* **2006**, *48*, 325–359. [CrossRef]
18. Akhtar, A. Compression of zirconium single crystals parallel to the c-axis. *J. Nucl. Mater.* **1973**, *47*, 79–86. [CrossRef]
19. Akhtar, A.; Teghtsoonian, A. Plastic deformation of zirconium single crystals. *Acta Metall.* **1971**, *19*, 655–663. [CrossRef]
20. Dickson, J.; Craig, G. Room-temperature basal slip in zirconium. *J. Nucl. Mater.* **1971**, *40*, 346–348. [CrossRef]
21. Caillard, D.; Gaumé, M.; Onimus, F. Glide and cross-slip of a-dislocations in Zr and Ti. *Acta Mater.* **2018**, *155*, 23–34. [CrossRef]
22. Knezevic, M.; Beyerlein, I.J.; Nizolek, T.; Mara, N.A.; Pollock, T.M. Anomalous basal slip activity in zirconium under high-strain deformation. *Mater. Res. Lett.* **2013**, *1*, 133–140. [CrossRef]
23. Akhtar, A. Basal slip in zirconium. *Acta Metall.* **1973**, *21*, 1–11. [CrossRef]
24. Li, Y.; Po, G.; Cui, Y.; Ghoniem, N. Prismatic-to-basal plastic slip transition in zirconium. *Acta Mater.* **2023**, *242*, 118451. [CrossRef]
25. Kaschner, G.; Gray, G. The influence of crystallographic texture and interstitial impurities on the mechanical behavior of zirconium. *Metall. Mater. Trans. A* **2000**, *31*, 1997–2003. [CrossRef]
26. Devincre, B.; Kubin, L.; Lemarchand, C.; Madec, R. Mesoscopic simulations of plastic deformation. *Mater. Sci. Eng. A* **2001**, *309*, 211–219. [CrossRef]
27. Soo, P.; Higgins, G. The deformation of zirconium-oxygen single crystals. *Acta Metall.* **1968**, *16*, 177–186. [CrossRef]
28. Ferrer, F.; Barbu, A.; Bretheau, T.; Crépin, J.; Willaime, F.; Charquet, D. The effect of small concentrations of sulfur on the plasticity of zirconium alloys at intermediate temperatures. In *ECCOMAS 2002-Zirconium in the Nuclear Industry: Thirteenth International Symposium*; ASTM International: West Conshohocken, PA, USA, 2001; Volume STP11420S, pp. 863–887. [CrossRef]
29. Allais, L.; Bornert, M.; Bretheau, T.; Caldemaison, D. Experimental characterization of the local strain field in a heterogeneous elastoplastic material. *Acta Metall. Mater.* **1994**, *42*, 3865–3880. [CrossRef]
30. Fundenberger, J.J.; Morawiec, A.; Bouzy, E.; Lecomte, J.S. System for creating orientation maps using TEM. *Mater. Chem. Phys.* **2003**, *81*, 535–537. [CrossRef]
31. Fundenberger, J.J.; Morawiec, A.; Bouzy, E. Advances in automatic TEM based orientation mapping. *Solid State Phenom.* **2005**, *105*, 37–42. [CrossRef]
32. Bunge, H. *Texture Analysis in Materials Science*; Butterworth-Heinemann: Oxford, UK, 1982; Volume 11, p. L0. [CrossRef]
33. Edington, J.W.; Edington, J. *Electron Diffraction in the Electron Microscope*; Springer: Berlin/Heidelberg, Germany, 1975. [CrossRef]
34. Zhang, Y.; Wang, S.; Esling, C.; Lecomte, J.S.; Schuman, C.; Zhao, X.; Zuo, L. A method to identify dislocations in a known crystal structure by transmission electron microscopy. *J. Appl. Crystallogr.* **2011**, *44*, 1164–1168. [CrossRef]
35. Bachmann, F.; Hielscher, R.; Schaeben, H. Grain detection from 2d and 3d EBSD data—Specification of the MTEX algorithm. *Ultramicroscopy* **2011**, *111*, 1720–1733. [CrossRef]
36. Beausir, B.; Fundenberger, J. Analysis Tools for Electron and X-ray diffraction, ATEX-software. *Univ. De Lorraine-Metz* **2017**, *2017*.
37. Fisher, E.; Renken, C. Single-crystal elastic moduli and the hcp→ bcc transformation in Ti, Zr, and Hf. *Phys. Rev.* **1964**, *135*, A482. [CrossRef]
38. Knezevic, M.; Zecevic, M.; Beyerlein, I.J.; Bingert, J.F.; McCabe, R.J. Strain rate and temperature effects on the selection of primary and secondary slip and twinning systems in HCP Zr. *Acta Mater.* **2015**, *88*, 55–73. [CrossRef]
39. An, X.; Zhang, H.; Ni, S.; Ou, X.; Liao, X.; Song, M. Effects of temperature and alloying content on the phase transformation and $\{10\bar{1}1\}$ twinning in Zr during rolling. *J. Mater. Sci. Technol.* **2020**, *41*, 76–80. [CrossRef]

40. Pujol, C. Etude des Mecanismes de Deformation en Traction et Fluage du zr Alpha Entre 20 et 300c. Ph.D. Thesis, ENMP, Paris, France, 1994.
41. Skippon, T.; Mareau, C.; Daymond, M. On the determination of single-crystal plasticity parameters by diffraction: Optimization of a polycrystalline plasticity model using a genetic algorithm. *J. Appl. Crystallogr.* **2012**, *45*, 627–643. [CrossRef]
42. Gong, J.; Britton, T.B.; Cuddihy, M.A.; Dunne, F.P.; Wilkinson, A.J. <a> Prismatic, <a> basal, and <c + a> slip strengths of commercially pure Zr by micro-cantilever tests. *Acta Mater.* **2015**, *96*, 249–257. [CrossRef]
43. Monnet, G.; Devincre, B.; Kubin, L. Dislocation study of prismatic slip systems and their interactions in hexagonal close packed metals: Application to zirconium. *Acta Mater.* **2004**, *52*, 4317–4328. [CrossRef]
44. Kelly, A.; Knowles, K.M. *Crystallography and Crystal Defects*; John Wiley & Sons: Hoboken, NJ, USA, 2020. [CrossRef]